CALPHAD: Computer Coupling of Phase Diagrams and Thermochemistry 85 (2024) 102702

Contents lists available at ScienceDirect

Calphad

journal homepage: www.elsevier.com/locate/calphad

Combined experimental and CALPHAD investigation of equimolar AlCoCrFeNiX (X=Mo,Ta,W) High-Entropy Alloys

S. Gambaro [a,*], L. Fenocchio [b], F. Valenza [a], P. Riani [b], G. Cacciamani [a,b]

[a] National Research Council, Institute of Condensed Matter Chemistry and Technologies for Energy, CNR-ICMATE, Genoa, 16149, Italy
[b] Chemistry and Industrial Chemistry Department (DCCI), University of Genova, Via Dodecaneso 31, 16146, Genoa, Italy

ARTICLE INFO

Handling Editor: Prof. Z.K. Liu

Keywords:
High-entropy alloys
Microstructure
CALPHAD approach
Phase equilibria

ABSTRACT

Aiming to evaluate the effect of refractory metal additions to a quinary AlCoCrFeNi High-Entropy Alloy (HEA), three novel equimolar AlCoCrFeNi-X (X = Mo, Ta, W) HEAs were designed, arc-melted, annealed, and characterized by SEM-EDS, XRD and microhardness measurements. CALPHAD thermodynamic calculations were exploited to design compositions and thermal treatments of the selected HEAs as well as to predict constitution and interpret microstructure of the samples. On the other hand, the experimental results contributed to the validation of the in-house built GHEA thermodynamic database (including the Al, Co, Cr, Fe, Ni, Mo, Ta, W elements) used for the calculations. No TCP intermetallic was found to form in the quinary AlCoCrFeNi alloy. However, the formation of σ, Laves-C14 and μ phases was observed in the samples containing Mo, Ta, and W, respectively, in agreement with the most accepted VEC-based phases stabilization criteria. The addition of the refractory metals led to a microhardness increase for all the investigated alloys. Overall, good agreement was observed between experiments and calculations, especially for compositional trends and phase amounts, allowing the database validation and supporting its applicability to phase equilibria simulation in the six-component HEAs belonging to the Al–Co–Cr–Fe–Ni-X (X = Mo, Ta, W) systems.

1. Introduction

During the last two decades, a new class of metallic materials, named High-Entropy Alloys (HEAs) or Multi-Principal-Element Alloys (MPEAs), has been proposed and deeply investigated as a possible replacement of conventional Ni- and Co-based superalloys currently used in nuclear, turbine and aerospace industries [1,2]. When introduced, the name HEA strictly referred to nearly equimolar solid solutions of five or more elements stabilized by the increased ideal entropy of mixing. Nowadays (and in this paper), the name HEA commonly refers to multicomponent alloys at quasi equimolar composition, independently on their single or multiphase constitution. Current HEAs, generally composed by a main solid solution and smaller amounts of secondary phases, often show exceptional mechanical properties [3], such as high hardness and ability to maintain their strength at elevated temperatures [4], excellent oxidation resistance [5], wear resistance [6], corrosion resistance and relevant yield strength, close to that of bulk metallic glasses (BMGs) [7]. However, differently to these latter, HEAs retain their high strength at more elevated temperatures when containing significant amounts of refractory elements such as Mo, Ta and W [8]. Such interesting properties make HEAs promising materials for the aerospace industry and, in general, for applications at high temperature and in aggressive environments. Among the broad family of HEAs, the equimolar AlCoCrFeNi quinary alloy was considered a promising structural material due to its appealing mechanical properties such as high compressive yield stress, compressive strength, and reasonable compressive ductility [2,9] accompanied with excellent corrosion and oxidation resistance [10]. Refractory metals such as Mo [11] and Ta [12] were added to alloys of this kind, aiming to improve their high temperature performances, even if the prediction of their effect on the final materials is complicated by the high number of interacting elements. Mo was found to change phase formation order, mole fraction and composition of the equilibrium phases in $Al_{0.5}CoCrFeMo_xNi$ and $CoCrFeNiMo_x$ alloys, favoring the formation of the σ phase, and increasing their hardness and compressive strength [11,13]. A similar effect was obtained when Ta was added to equimolar CoCrFeNi alloys; the resulting eutectic $CoCrFeNiTa_{0.4}$ HEA displayed higher fracture strength and compression than the starting alloy [14,15]. Non-equimolar $(AlTa_{0.76})_xCoCrFeNi_{2.1}$ and $AlCoCrFeNiTa_x$ HEAs were designed and characterized, showing phases and mechanical properties strictly related to the Ta content [16,17].

* Corresponding author.
E-mail address: sofia.gambaro@cnr.it (S. Gambaro).

https://doi.org/10.1016/j.calphad.2024.102702
Received 15 February 2024; Received in revised form 18 April 2024; Accepted 4 May 2024
Available online 11 May 2024
0364-5916/© 2024 The Authors. Published by Elsevier Ltd. This is an open access article under the CC BY license (http://creativecommons.org/licenses/by/4.0/).

Finally, the addition of W to CoCrFeNi alloys was found to promote the μ phase formation, so that the resulting $CoCrFeNiW_x$ alloys are composed of an FCC matrix, strengthened by the precipitation of such topologically close packed (TCP) phase [18,19]. Other investigations were carried out on alloys at the $AlCoCrFeNi_2W_x$ and $Al_{1-x}CoCrFeNi_2W_x$ compositions, whose FCC + BCC microstructure and mechanical properties revealed to be tunable with the Al/W ratio [20,21]. Even if, as mentioned above, several alloys in the Al–Co–Cr–Fe–Ni-X (X = Mo, Ta, W) systems have already been investigated in the literature, to the best of our knowledge no work has been conducted on the characterization of the equiatomic AlCoCrFeNiX (X = Mo, Ta, W) compositions which are particularly relevant for the validation of a thermodynamic database.

In the present work, three senary AlCoCrFeNiX (X = Mo, Ta, W) alloys were synthesized and characterized. Additionally, a fourth AlCoCrFeNi quinary sample was prepared as a reference to evaluate the effect of the different refractory element additions. The experimental investigation was combined with thermodynamic modelling, according to the CALPHAD approach. It is well known that CALPHAD calculations are an effective tool to forecast phase equilibria in HEA systems [22]. These calculations are particularly challenging for HEAs, since a database including many elements and covering wide composition ranges is required for the proper modelling of such multi-component and multi-phase systems. Nevertheless, several successful examples of CALPHAD approach as a tool to accelerate design and characterization of new HEAs exist in the literature [23–26]. In this framework, a CALPHAD thermodynamic database named GHEA (Genova High-Entropy Alloys) is being developed at the University of Genova. Over the years, GHEA has been used to simulate metallic coatings [27], Co-based superalloys [28], and HEAs [29,30]. In all cases, comparisons with experimental results from such investigations have been used to validate and further improve the thermodynamic database itself. In this work, GHEA has been used as a fundamental tool to design sample preparation procedure (especially equilibration temperatures) and interpret phase analysis results. Experimental data also played a key role; in fact, the comparison between predictions and measurements has been used to validate the database, supporting its future development.

2. Materials and method

2.1. Samples preparation and characterization

In this work, four equiatomic alloys AlCoCrFeNi, AlCoCrFeNiMo, AlCoCrFeNiTa and AlCoCrFeNiW, hereafter referred to as HEA-Ref, HEA-Mo, HEA-Ta, and HEA-W, respectively, were synthesized by arc-melting. It has to be noted that for such refractory-rich, Al-containing HEAs this procedure is usually complicated; the boiling temperature of Al is lower than the melting point of the refractory metals, possibly causing Al losses or the presence of unreacted Mo, Ta, or W. For this reason, selected binary and ternary alloys were preliminarily prepared by arc-melting the appropriate quantities of the pure metals (purity > 99.9 %), and then combined to obtain the final senary alloys. The slight differences between nominal and experimental compositions (see Table 3 and the final discussion) can be attributed to such 2-steps preparation. Arc-melting was performed under purified Ar atmosphere and the oxygen content in the chamber was further reduced by arc-melting a piece of Zr before each melting process; to ensure compositional homogeneity, the alloys were flipped and re-melted up to 10 times. Alloy samples of about 0.5 g were obtained. After arc-melting, to ensure equilibration, samples were wrapped in Ta foils, closed in quartz vials under inert atmosphere, annealed and finally quenched in water. Duration and temperatures of the treatments were specifically selected for each sample with the aid of thermodynamic calculations performed with the GHEA database (details are reported in Table 3). In view of the micrographic observation, cross-sectioned samples were mechanically polished down to 1 μm using diamond paste. Sample microstructure and phase compositions were analyzed by SEM (model: LEO 1450 VP) coupled with EDS (Oxford Instruments, 7353 model with Oxford-INCA software v.4.07, type detector: Si(Li)). Phase amounts in mole fraction (of atoms) were qualitatively evaluated assuming that they are equivalent to the volume fractions determined by image analysis (software GIMP) of the alloy surfaces observed by SEM. The assumed equivalence between volume and mole fractions is justified by the small variation between the molar volumes of metals and alloys. XRD analysis was performed using a powder diffractometer (Siemens D-500 - CuK_α radiation, Ni filter; operated in the vertical mode on 40 kV and 30 mA) equipped with the Diffract AT V3 software package. X-ray patterns were collected in the 30–100° 2θ range. XRD was carried out on the polished surface of bulk samples, since it was impossible to obtain powder of sufficient quality. Finally, microhardness of the different phases in the samples was measured using a Vickers indenter (Leica VM HT MOT), with a load of 0.01 kgf (0.098 N) and a dwell time of 12 s; additional indentations were performed at higher loads, 0.1 kgf (0.98 N), aiming to evaluate the contribute of the different phases to the global microhardness of the alloy. At least 5 indentations were performed for each measurement. The distance between the different indentations was taken to be higher than three times the length of their diagonal.

2.2. CALPHAD approach

The Al–Co–Cr–Fe–Ni–Mo–Ta–W thermodynamic database used in this work is a subset of GHEA (Genova High-Entropy Alloys) [30], a larger CALPHAD thermodynamic database under continuous development at the University of Genova, by means of a recursive expansion and experimental validation procedure of which this work is also a part. The Al–Co–Cr–Fe–Ni 5-component database was validated by comparing calculations with experimental data from literature and from key experiments conducted by Ostrowska et al. [29]. Later, new elements such as Mo, Ta and W were added by Ostrowska during her Ph.D. Thesis [31].

Table 1
Sublattice models of the most important phases appearing in the Al–Co–Cr–Fe–Ni-X (X = Mo, Ta, W) systems.

Phase	Structure	Sublattice Model
FCC-A1 (a)	*cF4* – Cu	$(Al,Co,Cr,Fe,Ni,X)_1$ $(Va)_1$
FCC4 ($L1_2$ and $L1_0$)	cP4 – $AuCu_3$	$(Al,Co,Cr,Fe,Ni,X)_{0.25}$ $(Al,Co,Cr,Fe,Ni,X)_{0.25}$
	tP4 – AuCu	$(Al,Co,Cr,Fe,Ni,X)_{0.25}$ $(Al,Co,Cr,Fe,Ni,X)_{0.25}$ $(Va)_1$
BCC-A2 (b)	*cI2* – W	$(Al,Co,Cr,Fe,Ni,X)_1$ $(Va)_3$
BCC-B2	*cP2* – CsCl	$(Al,Co,Cr,Fe,Ni,X)_{0.5}$ $(Al,Co,Cr,Fe,Ni,X)_{0.5}$ $(Va)_3$
HCP-A3	*hP2* – Mg	$(Al,Co,Cr,Fe,Ni,X)_1$ $(Va)_{0.5}$
Laves-C15	*cF24* – $MgCu_2$	$(Al,Co,Cr,Fe,Ni,X)_1$ $(Al,Co,Cr,Fe,Ni,X)_2$
Laves-C14	*hP12* – $MgZn_2$	$(Al,Co,Cr,Fe,Ni,X)_1$ $(Al,Co,Cr,Fe,Ni,X)_2$
Laves-C36	*hP24* – $MgNi_2$	$(Al,Co,Cr,Fe,Ni,X)_1$ $(Al,Co,Cr,Fe,Ni,X)_2$
σ	*tP30* – CrFe	$(Al,Co,Cr,Fe,Ni,X)_2$ $(Al,Co,Cr,Fe,Ni,X)_8$ $(Al,Co,Cr,Fe,Ni,X)_5$
μ	*hR36* – W_6Fe_7	$(Al,Co,X)_4$ $(Al,Co,Cr,Fe,Ni,X)_2$ $(Al,Co,Cr,Fe,Ni,X)_1$ $(Al,Co,Cr,Fe,Ni,X)_6$

(a) disordered contribution to FCC4.
(b) disordered contribution to BCC-B2.

Overall, more than 200 phases are modeled in GHEA. Thermodynamic models adopted for the most important phases appearing in the binary and ternary subsystems of Al–Co–Cr–Fe–Ni-X (X = Mo, Ta, W) were introduced and discussed by Ostrowska [29,31] and are summarized in Table 1.

All binary and ternary subsystems of Al–Co–Cr–Fe–Mo–Ni, Al–Co–Cr–Fe–Ni–Ta and Al–Co–Cr–Fe–Ni–W have been thermodynamically assessed in GHEA. Binary and ternary interaction parameters, when available, have been initially taken from literature and, when necessary, modified to be consistent with phase models and lower order systems adopted in GHEA. Special attention has been given to the evaluation of metastable (or unstable) endmembers, including lattice stabilities of the pure elements in their metastable structures as well as binary and ternary endmembers of the solution phases: generally, DFT values have been preferred to the arbitrary values frequently adopted in older literature. Moreover, it was often necessary to reassess binary endmembers common to more ternary systems and differently evaluated in the literature. The addition of Mo, Ta, and W (here denoted by X) to the database which included Al, Co, Cr, Fe, Ni (here denoted by M) required the assessment of all binary M-X and ternary M1-M2-X systems. They are listed in Table 2, together with some details about the assessment procedure. A more complete and in-depth presentation of GHEA, including a discussion of the adopted phase models, endmember energies, assessment procedures, etc. will be presented in an upcoming paper.

3. Results and discussion

Four key alloys, namely HEA-Ref, HEA-Mo, HEA-Ta and HEA-W, were synthesized by arc-melting followed by annealing and water-quenching. Their microstructures are shown in Fig. 1 and discussed in the following sections. Details on the thermal treatments and global compositions of the samples are reported in Table 3. For each sample, the annealing temperature was chosen to be about 100 °C below the solidus temperature predicted by GHEA, aiming to equilibrate the alloys at the highest possible temperature, while avoiding the formation of liquid phase during the heat treatment. A 100 °C margin was selected as a reasonable choice, considering uncertainties coming from both experimental procedures and predicted melting temperatures.

As for the HEA-W sample, the annealing was performed at 950 °C aiming to obtain a homogeneous microstructure without any reprecipitated elemental W (BCC-A2 phase in Fig. 9). To ensure equilibration at such annealing temperature, a longer treatment was performed for this sample (25 d vs 15 d for the other alloys).

In the following sections, for each sample, experimental results (SEM-EDS, XRD, image and micro-hardness analyses) are reported and compared to the thermodynamic predictions calculated by means of the GHEA database. The calculations were performed considering the experimental compositions of the alloys as measured by SEM-EDS and reported in Table 3, rather than their nominal equiatomic compositions. This approach, consisting of reciprocal validation between experimental and calculated results, has been successfully adopted by the authors to predict and interpret other metallic and metal-ceramic samples after different thermal treatments [56–59].

3.1. Sample HEA-Ref equilibrated at 1250 °C

Three phases can be distinguished in the HEA-Ref alloy (Fig. 2): a darker and more abundant (Al,Ni)-based BCC-B2 phase, a brighter (Cr, Fe)-rich FCC-A1 phase and a gray Cr-rich BCC-A2 phase (A, B and C regions in Fig. 2a and blue, red, and green regions in Fig. 2b, respectively). BCC-B2 forms large crystals, surrounded by FCC-A1, while BCC-A2 seems to have mainly grown during annealing. The phases were confirmed by XRD analysis (Fig. 2c). Notice that BCC-A2 peaks appear as shoulders on the left side of the BCC-B2 peaks (except for that at $2\theta = 31^{\circ}$, typical only of the ordered structure).

The equilibrium phase fraction (EPF) vs temperature plot calculated by means of GHEA for the experimental alloy composition is reported in Fig. 3. According to the performed calculations, BCC-B2 is the first phase solidifying from the liquid during cooling at about 1370 °C, followed by FCC-A1 at about 1360 °C. Finally, BCC-A2 is predicted to form in the solid state at about 920 °C (Fig. 3).

Phase amounts calculated at the equilibration temperature of 1250 °C are compared in Table 4 to those determined by image analysis of the SEM micrograph (Fig. 2b). According to the calculations BCC-A2 is not stable at 1250 °C; nevertheless, it is present in the sample. This disagreement probably indicates that GHEA underestimates the stability of BCC-A2 in this alloy. However, a better agreement between experiments and calculations is obtained if calculated amount and composition of B2 are compared to the experimental results for the sum of A2 and B2 (see Table 4). Finally, it can be noticed that qualitative agreement is obtained for the FCC-A1 phase. General considerations on the agreement between calculated and experimental compositions for all the samples are further discussed in section 4.

Table 2
Binary M-X (M = Al, Co, Cr, Fe, Ni; X = Mo, Ta, W) and ternary M1-M2-X systems included in GHEA. Details on the assessment procedure are reported.

Binary systems		Ternary systems	
System	Interaction parameters based on	System	Assessment procedure
Al–Mo	[32,33]	Al–Co–Mo, Al–Co–Ta, Al–Ni–Ta, Co–Ni–Ta, Cr–Ni–Ta, Cr–Fe–Mo, Cr–Ni–Mo, Fe–Ni–Mo, Fe–Ni–Ta	New assessment or reassessment in GHEA
Al–Ta	[34]	Al–Cr–Mo, Al–Cr–Ta, Al–Cr–W, Al–Fe–W, Co–Fe–Ta, Cr–Fe–Ta	Ideal combination of the binary subsystems
Al–W	[35]	Al–Co–W	Adapted from [35]
Co–Mo	[36]	Al–Fe–Mo	Adapted from [37]
Co–Ta	[38]	Al–Fe–Ta	Adapted from [39]
Co–W	[35]	Al–Ni–Mo	Adapted from [33]
Cr–Mo	[40]	Al–Ni–W, Co–Ni–W	Adapted from [41]
Cr–Ta	[42,43]	Co–Cr–Mo	Adapted from [44]
Cr–W	[45]	Co–Cr–Ta	Adapted from [28]
Fe–Mo	[46]	Co–Cr–W	Adapted from [27]
Fe–Ta	[47]	Co–Fe–Mo	Adapted from [48]
Fe–W	[45,49]	Co–Fe–W, Fe–Ni–W	Adapted from [50]
Ni–Mo	[51]	Co–Ni–Mo	Adapted from [52]
Ni–Ta	[53]	Cr–Fe–W	Adapted from [45]
Ni–W	[54]	Cr–Ni–W	Adapted from [55]

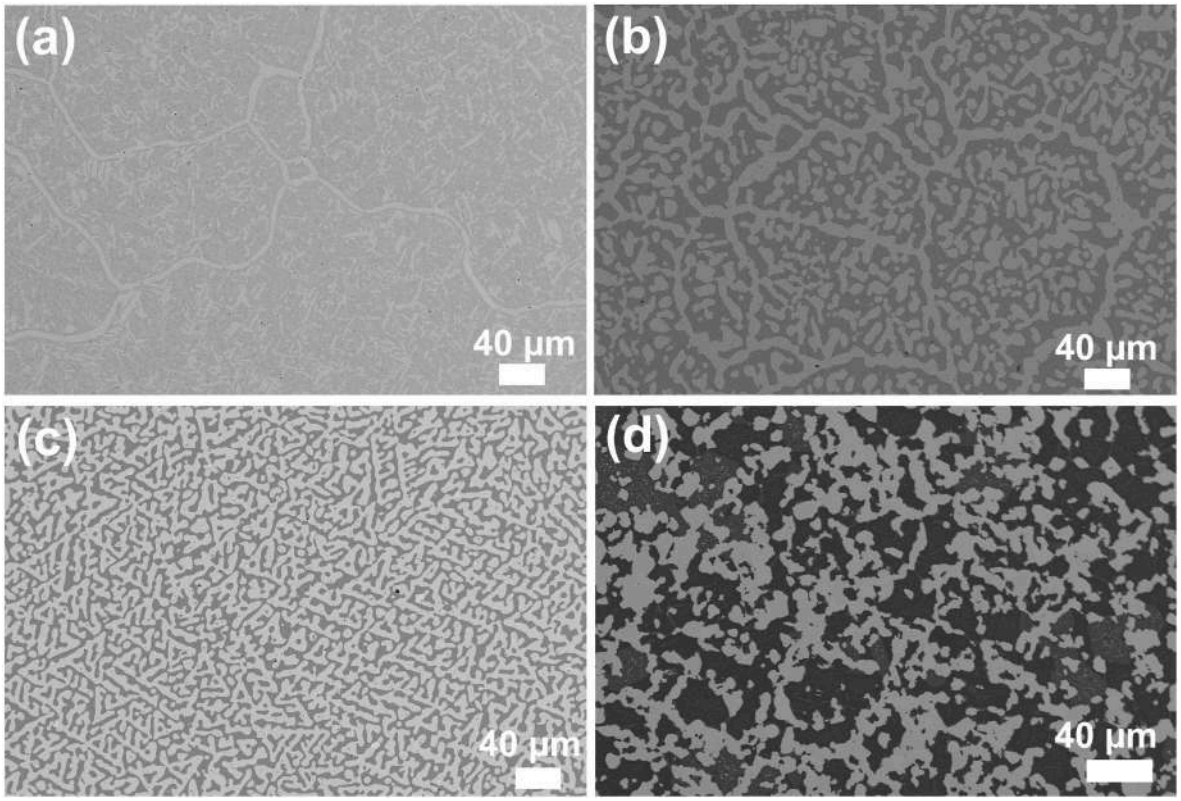

Fig. 1. BSE image of HEAs after equilibration (see Table 3): HEA-Ref (a); HEA-Mo (b); HEA-Ta (c); HEA-W (d).

Table 3
Thermal treatment and composition (mol%) determined by EDS of cross-sectioned HEA-Ref, HEA-Mo, HEA-Ta, HEA-W samples. The slight differences between nominal and experimental compositions can be attributed to the synthesis procedure (see Section 2.1). Additionally, calculated solidus and liquidus temperatures are reported.

Sample	HEA-Ref	HEA-Mo	HEA-Ta	HEA-W
Thermal treatment	1250 °C; 15 d	1150 °C; 15 d	1250 °C; 15 d	950 °C; 25 d
Solidus (°C)	~1350 °C	~1230 °C	~1340 °C	~1310 °C
Liquidus (°C)	~1380 °C	~1300 °C	~1580 °C	~1825 °C
Al	19.1	17.8	15.6	14.2
Co	20.2	17.7	16.9	17.2
Cr	20.6	17.1	16.2	13.0
Fe	19.7	17.0	16.1	15.0
Ni	20.4	18.2	18.8	23.8
Mo	–	12.2	–	–
Ta	–	–	16.4	–
W	–	–	–	16.8

3.2. Sample HEA-Mo equilibrated at 1150 °C

Two phases were experimentally observed in the HEA-Mo alloy; a darker (Al,Ni)-rich BCC-B2 primary phase (label D in Fig. 4a, blue in Fig. 4b) surrounded by a lighter (Cr,Mo)-rich σ phase (label E in Fig. 4a, orange in Fig. 4b).

Phases amounts were determined by image analysis (Fig. 4b) and their identities were confirmed by XRD measurements (Fig. 4c). Also in this case, the EPF vs temperature plot was calculated by means of the GHEA database (Fig. 5).

From calculations, BCC-B2 is the first phase solidifying from the liquid at about 1300 °C, followed by the σ phase forming at about 1230 °C, when the liquid disappears. Finally, the μ phase forms at about 900 °C from a solid-state reaction (Fig. 5). At the annealing temperature of 1150 °C the calculated equilibrium situation is that of a two-phase microstructure with 68 mol% of BCC-B2 and 32 mol% of σ phase. Calculated and experimental phase amounts and compositions, compared in Table 5, show a satisfactory agreement, further discussed in section 4.

3.3. Sample HEA-Ta equilibrated at 1250 °C

The microstructure of the HEA-Ta alloy is mostly biphasic, being composed of a lighter (Cr,Ta)-rich Laves-C14 primary phase (G in Fig. 6a, orange in Fig. 6b) surrounded by a darker (Al,Ni)-rich BCC-B2 phase (F in Fig. 6a, blue in Fig. 6b). In addition, a very small quantity of a third unidentified phase is present, labeled G′ since it only appears inside G. Phase amounts determined by image analysis (Fig. 6b) are reported in Table 6. The presence of the Laves-C14 phase was confirmed by XRD analysis (Fig. 6c). As for BCC-B2, the typical superstructure peak at 31° is hardly visible due to the high intensity of the nearby peak of Laves-C14. However, considering the EDS measured composition of BCC-B2 (rich in Al and Ni) and the indications coming from calculations, it was possible to confirm the presence of BCC-B2. The experimental identification of the G' phase was instead not possible, due to its small amount. According to the calculated EPF vs temperature plot (Fig. 7), the Laves-C14 phase is the first solidifying from the liquid at about 1580 °C while the secondary (Al,Ni)-rich BCC-B2 phase precipitates at 1370 °C. At about 1125 °C a second (Ta,Ni)-rich Laves-C14 phase is predicted to form from that already present; its composition calculated just below the formation temperature is 17 mol% Al, 11 mol% Co, 2 mol % Cr, 5 mol% Fe, 32 mol% Ni and 33 mol% Ta.

The calculated equilibrium at 1250 °C predicts a two-phase situation with 48 mol% of the Laves-C14 primary phase and 52 mol% of BCC-B2. Phase analysis results are compared with thermodynamic calculations in Table 6.

Considering both phase amounts and compositions, a satisfactory agreement can be observed between experimental measurements and calculated results (further discussed in section 4), even if some

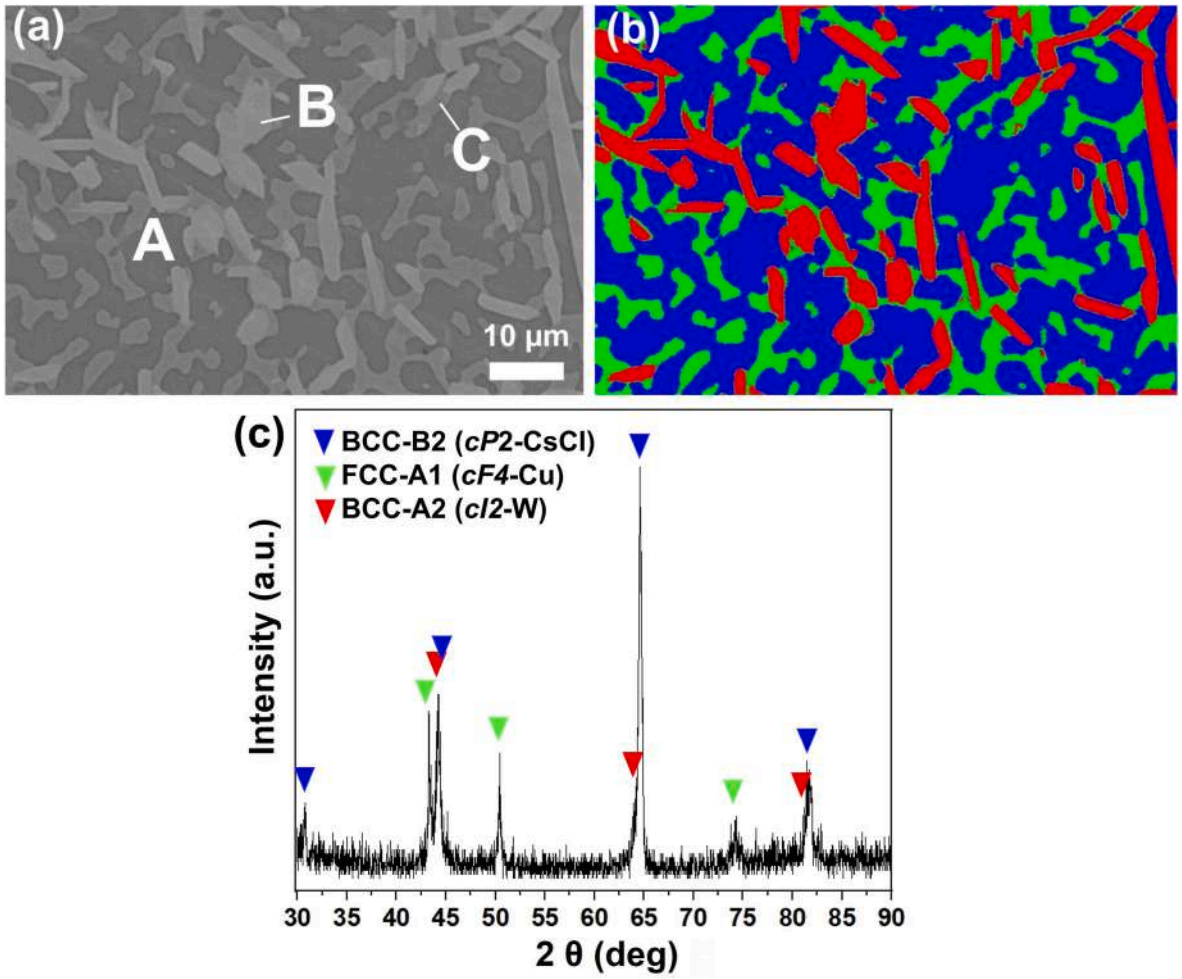

Fig. 2. HEA-Ref sample after annealing: microstructure by BSE (a); phases recognition by image analysis (b); XRD diffraction pattern (c).

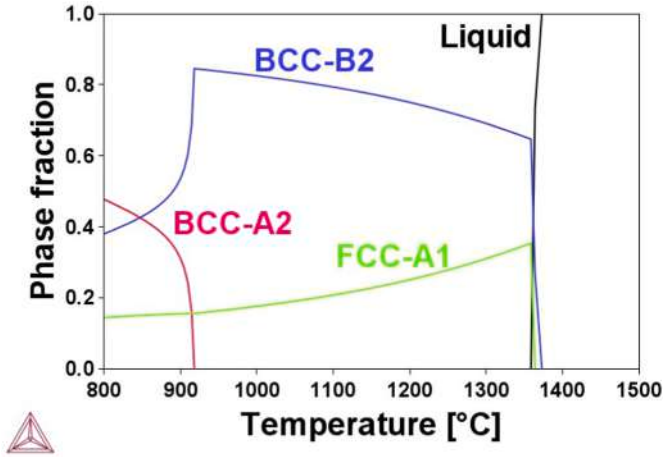

Fig. 3. Equilibrium phase fraction (EPF) vs temperature plot for the HEA-Ref sample.

discrepancies exist, especially for Co and Fe in both the Laves-C14 and BCC-B2 phases. Moreover, calculations suggest that the third unidentified phase (G' of Fig. 6a) probably corresponds to the (Ta,Ni)-rich Laves-C14 phase, unstable at the annealing temperature but able to precipitate during quenching, even if in very small quantity.

Table 4
– *Comparison between experimental and calculated* equilibrium phase fraction *(EPF, mol%) and compositions (mol%) of the phases detected in the HEA-Ref sample equilibrated at 1250°C.*

Phase		EPF	Al	Co	Cr	Fe	Ni
BCC-B2 (A of Fig. 2a)	EXP	57.1	32.3	12.4	7.3	18.8	29.2
	CALC	72.3	21.4	18.8	18.7	20.6	20.5
A2 + B2	EXP	76.7	24.5	13.4	18.0	21.2	22.8
FCC-A1 (B of Fig. 2a)	EXP	23.3	5.5	23.7	28.4	29.0	13.3
	CALC	27.7	13.2	23.9	25.5	17.3	20.1
BCC-A2 (C of Fig. 2a)	EXP	19.6	1.8	16.4	49.2	28.4	4.2

3.4. Sample HEA-W equilibrated at 950 °C

The annealing temperature of 950 °C chosen for this sample (much lower than the expected solidus temperature of ~ 1310 °C) was selected to avoid formation of the W-based BCC-A2 phase, predicted to be stable from high temperature down to ~ 960 °C. We suspected that the presence of this very stable phase would complicate the attainment of the equilibrium during the solid-state annealing. To ensure equilibration at this lower temperature, a longer heat treatment was performed, annealing the sample for 25 days (instead of the 15 days chosen for the other alloys). The microstructure of the so obtained HEA-W alloy is composed of three phases; a lighter W-rich μ phase (L in Fig. 8a, orange in Fig. 8b), and two different darker phases which correspond to the (Al, Ni)-rich BCC-B2 (H in Fig. 8a, blue in Fig. 8b) and the (Co,Fe,Ni)-rich FCC-A1 (I in Fig. 8a, green in Fig. 8b) phases. The identities of the FCC-

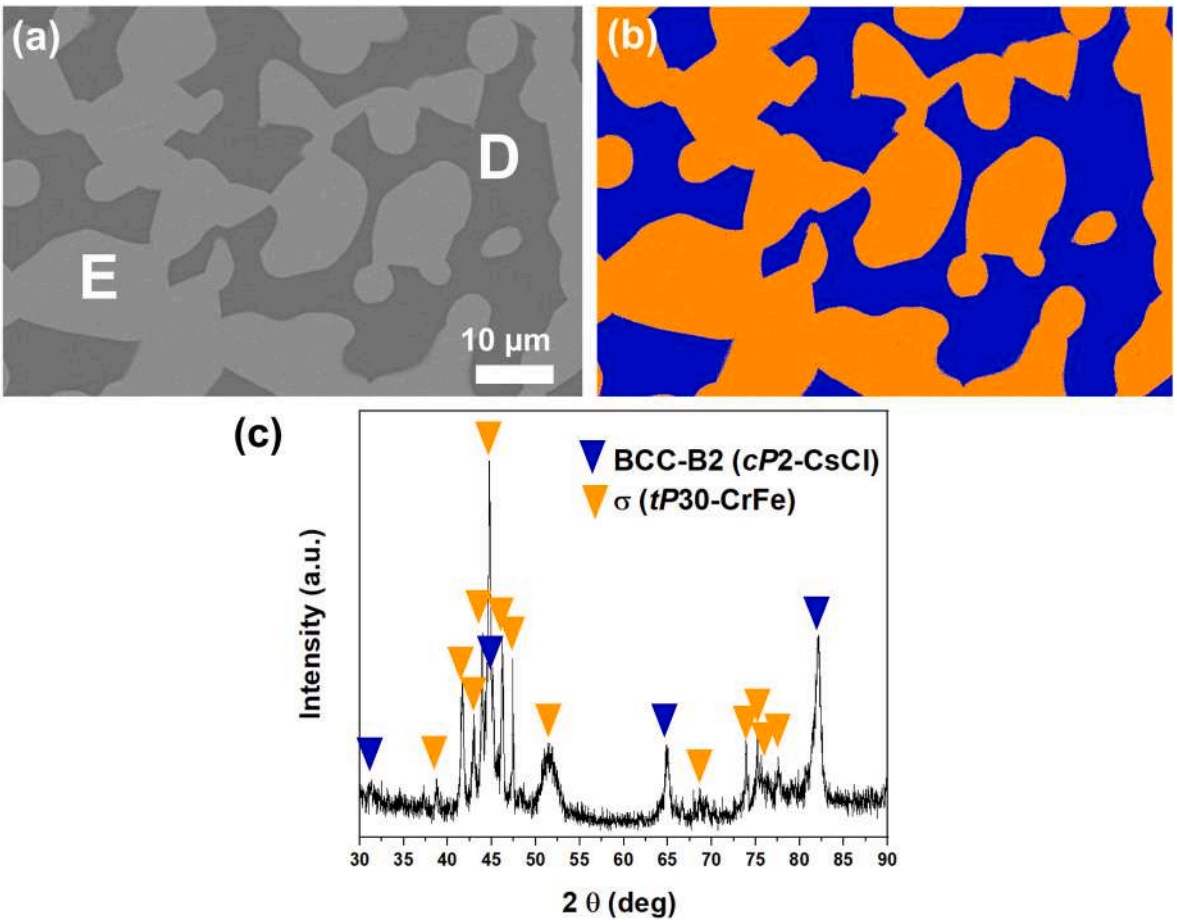

Fig. 4. HEA-Mo sample after annealing: microstructure by BSE (a); phases recognition by image analysis (b); XRD diffraction pattern (c).

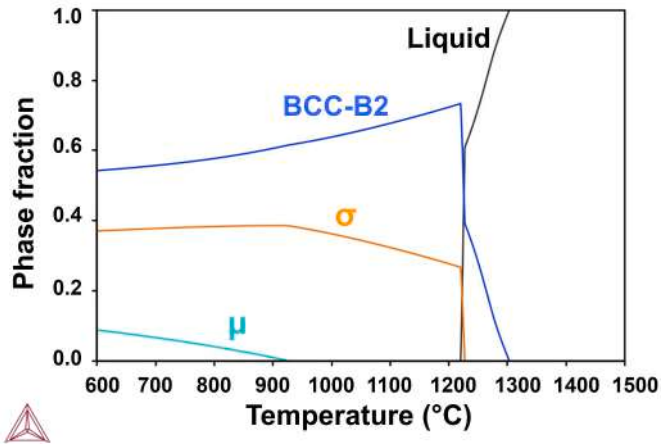

Fig. 5. Equilibrium phase fraction (EPF) vs temperature plot for the HEA-Mo sample.

A1 and μ phases were confirmed by XRD analysis (Fig. 8c). As for BCC-B2, similarly to HEA-Ta, its presence was reasonably confirmed by both calculations and EDS composition, since the superstructure peak at 31° is not clearly visible. Finally, qualitative estimation of phase amounts was performed by image analysis (Fig. 8b).

The calculated EPF vs temperature plot reported in Fig. 9 well agrees with experimental observations; the three experimentally detected phases, namely μ, BCC-B2 and FCC-A1, correspond to those calculated in the equilibrium conditions for temperatures lower than 950 °C, while BCC-A2, stable at higher temperature, was not detected in the sample. Experimental and calculated results summarized in Table 7 are in fair agreement (further discussed in section 4).

Table 5
Comparison between experimental and calculated equilibrium phase fraction (EPF, mol%) and compositions (mol%) of the phases detected in the HEA-Mo sample equilibrated at 1150 °C.

Phase		EPF	Al	Co	Cr	Fe	Ni	Mo
BCC-B2 (D of Fig. 4a)	EXP	53.0	27.8	18.3	9.0	14.5	27.9	2.5
	CALC	68.0	27.2	16.9	10.8	18.0	27.1	–
σ (E of Fig. 4a)	EXP	47.0	5.3	17.7	27.4	20.6	7.8	21.2
	CALC	32.0	–	20.3	26.6	12.3	5.2	35.6

4. General considerations

4.1. Phases stability and composition

In agreement with predictions by GHEA, an (Al,Ni)-rich BCC-B2 phase was detected in all the investigated HEAs. The good agreement between experimental and calculated data also regards BCC-B2 compositions (Tables 4–7) and phase amounts (Fig. 10). In the particular case of HEA-Ref, the calculated amount of BCC-B2 is better compared to the sum of BCC-B2 + BCC-A2 detected in the sample, as discussed above.

BCC-B2 compositions measured in the different samples are compared in Table 8, resulting very similar to each other: the BCC-B2 phase forming in the samples containing the refractory element is the same forming in HEA-Ref. According to the calculations, BCC-B2 is based on the AlNi binary phase dissolving other components: mainly Fe

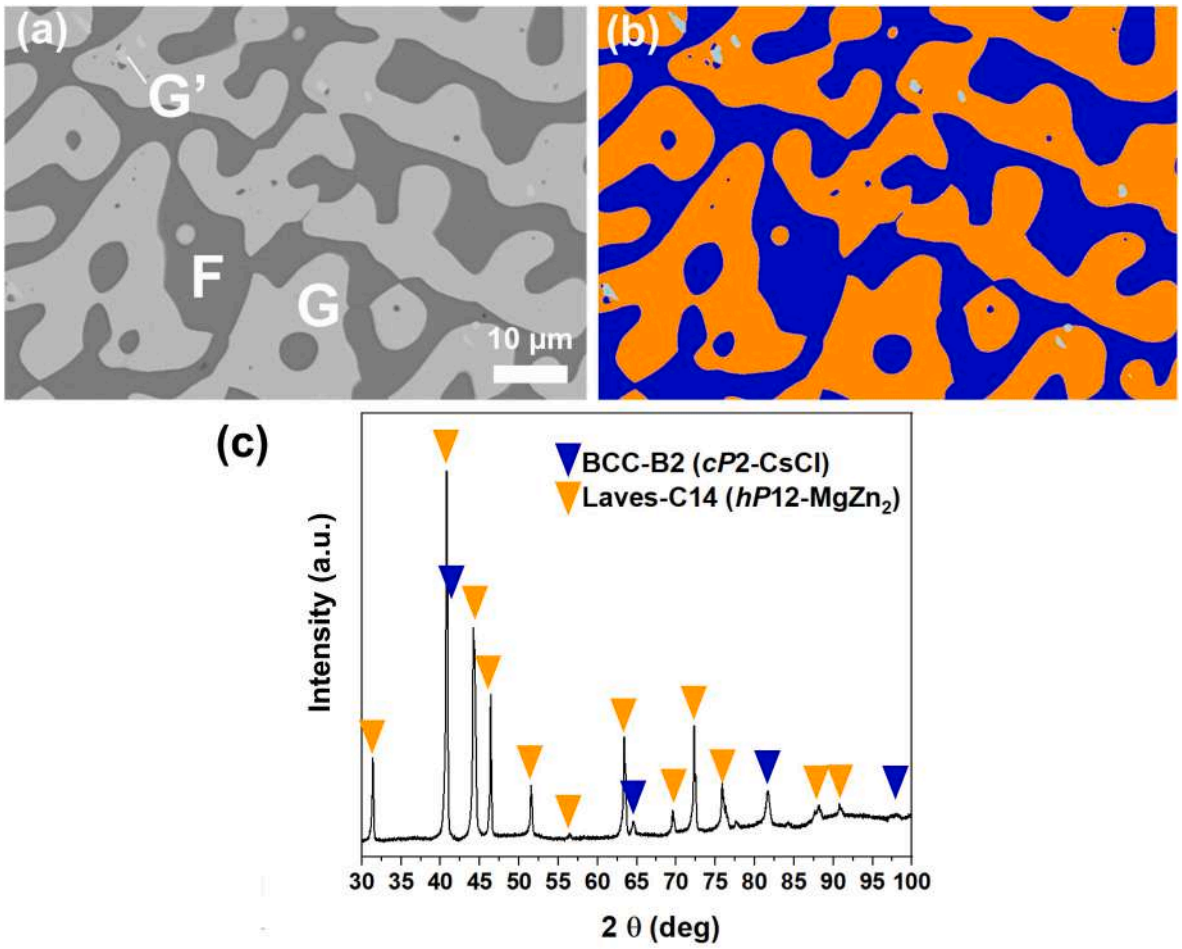

Fig. 6. HEA-Ta sample after annealing: microstructure by BSE (a); phases recognition by image analysis (b); XRD diffraction pattern (c).

Table 6
Comparison between experimental and calculated equilibrium phase fraction (EPF, mol%) and compositions (mol%) of the phases detected in the HEA-Ta sample equilibrated at 1250 °C.

Phase		EPF	Al	Co	Cr	Fe	Ni	Ta
BCC-B2 (F of Fig. 6a)	EXP	51.2	34.2	15.1	8.8	10.5	28.8	2.6
	CALC	52.0	27.7	4.9	9.3	23.6	30.7	3.7
Laves-C14 (G of Fig. 6a)	EXP	48.5	3.5	17.7	22.4	21.3	7.2	27.8
	CALC	48.0	–	32.3	24.9	6.5	0.0	32.3

in the Al sublattice, and mainly Co in the Ni sublattice, while Cr and the refractory element usually enter both sublattices in similar proportions. However, the refractory element is present in very limited quantity in the BCC-B2 phase (maximum concentration is 2.6 mol% in HEA-Ta), since it is mainly involved in the formation of a secondary phase (σ for Mo, Laves-C14 for Ta, and μ for W).

The Cr-based BCC-A2 solid solution does not appear in the alloys containing refractory elements. Only in the HEA-W sample a BCC-A2 phase is present at high temperature, but it corresponds to the W-based terminal solid solution. Based on this, it is possible that the GHEA database slightly overestimate the stability of BCC-B2 compared to that of the Cr-rich BCC-A2, but further confirmation is required. As for the TCP intermetallics, a different phase was stabilized in each alloy, depending on the added refractory element. The comparison between calculated and experimental EPF gave satisfactory results (Tables 4–7). Some discrepancies were observed in terms of phase compositions, especially for the σ and μ phases probably due to their higher number of sublattices in the model, resulting in a higher number of endmembers to

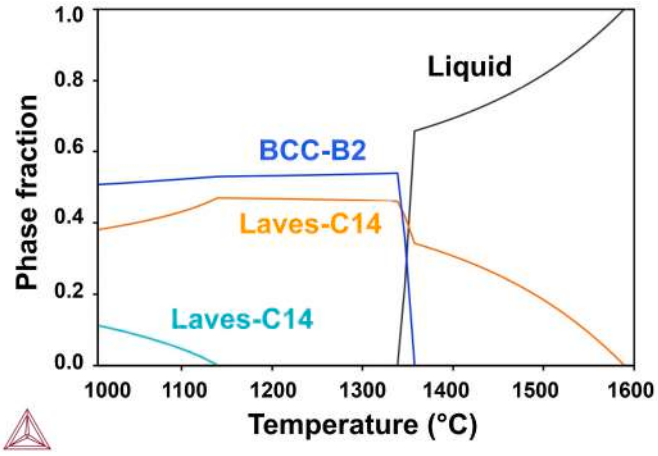

Fig. 7. Equilibrium phase fraction (EPF) vs temperature plot for the HEA-Ta sample.

evaluate, often in absence of literature data. Compositional similarities were found between these intermetallics: they contain a low amount of Al and Ni, which are mainly involved in the formation of the BCC-B2 solid solution, and the Co content is around 17–18 mol% (see Table 9). Moreover, some differences exist in the content of the refractory element, higher for the μ phase than for the other TCP.

As mentioned in section 3, some differences between calculated and experimental compositions can be observed, showing the following

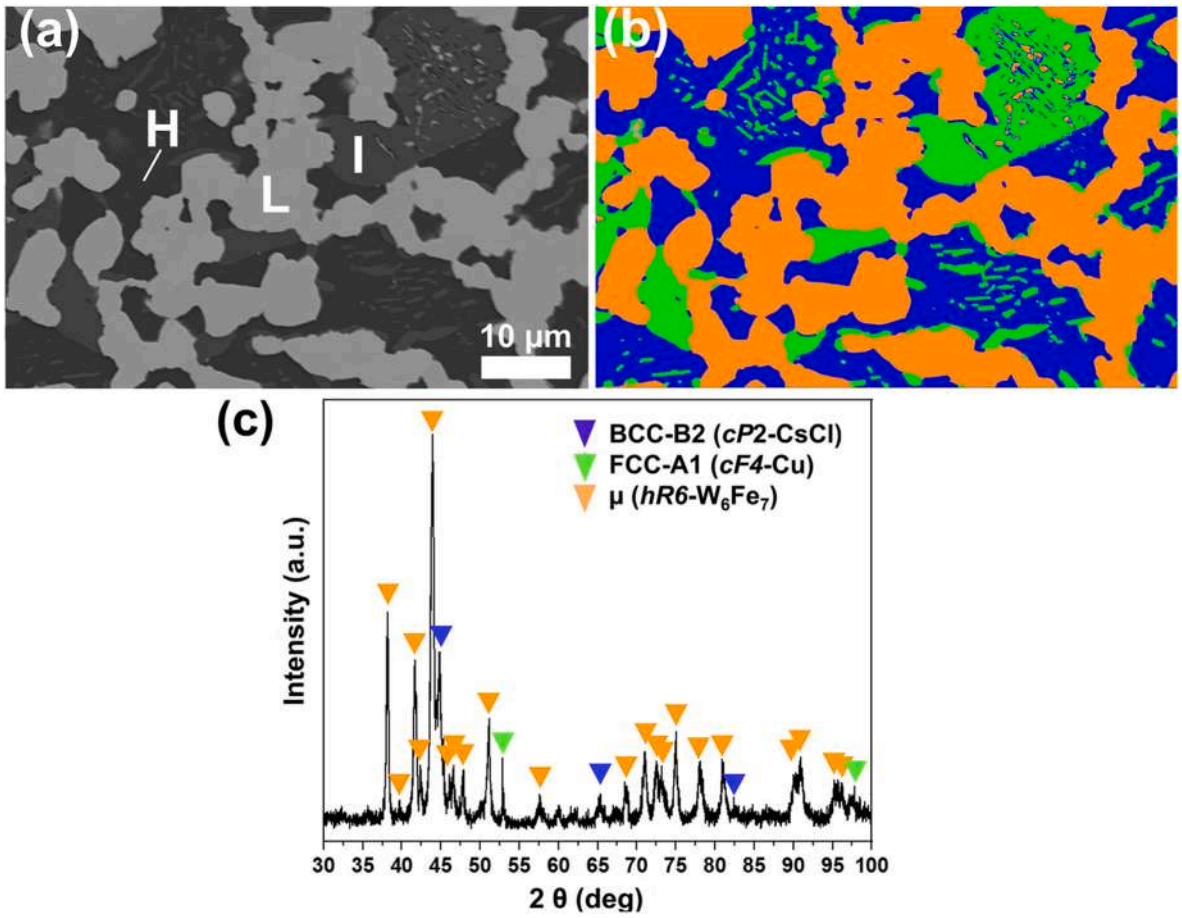

Fig. 8. HEA-W sample after annealing: microstructure by BSE (a); phases recognition by image analysis (b); XRD diffraction pattern (c).

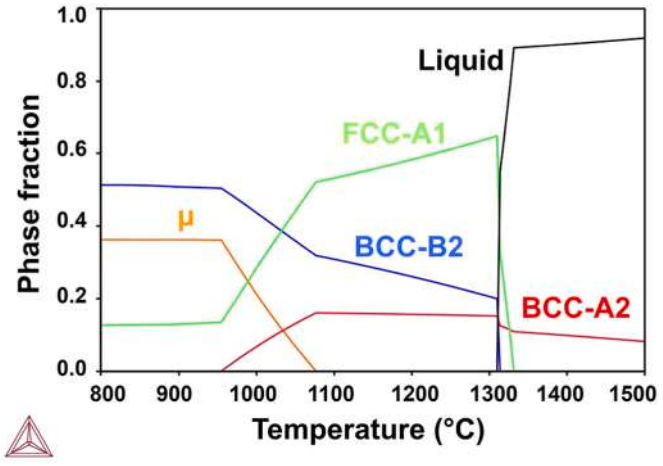

Fig. 9. Equilibrium phase fraction (EPF) vs temperature plot for the HEA-W sample.

systematic behaviors.

1) in FCC-A1, Ni is generally overestimated while Al, Co and Fe underestimated;
2) in BCC-B2, Cr and Fe are usually overestimated, while Co is underestimated when a refractory element is added to the alloy;
3) in TCP phases, Co and the refractory elements are overestimated while Al, Fe and Ni underestimated.

Table 7
Comparison between experimental and calculated equilibrium phase fraction (EPF, mol%) and compositions (mol%) of the phases detected in the HEA-W sample equilibrated at 950 °C.

Phase		EPF	Al	Co	Cr	Fe	Ni	W
BCC-B2 (H of Fig. 8a)	EXP	37.0	28.6	16.2	7.3	12.7	34.4	0.7
	CALC	51.0	25.9	12.1	10.5	17.6	33.8	–
FCC-A1 (I of Fig. 8a)	EXP	16.4	10.1	21.4	18.1	21.4	24.7	4.3
	CALC	11.5	10.3	17.9	22.3	18.9	29.3	1.5
μ (L of Fig. 8a)	EXP	46.6	1.7	17.1	18.7	16.0	6.7	39.8
	CALC	37.5	–	23.5	12.7	11.0	7.0	42.5

These systematic compositional discrepancies are probably related to the stabilities of the metastable endmembers of the mentioned phases. The behavior of Co, for instance, suggests that the stabilities of its endmembers in TCP phases are probably overestimated, so it appears that they should be slightly corrected. However, correcting the database based on one single composition might lead to a general decrease of the database reliability in other composition and temperature ranges. Corrections will be applied in the future considering a wider set of experimental data.

The stabilization of BCC and FCC structures in HEAs has been related to the overall valence electron concentration (VEC) of the alloys by Guo et al. [60]. They suggested that HEAs are monophasic BCC for VEC $<$ 6.7, and monophasic FCC for VEC $>$ 8.0, while they show bi- or multi-phasic combinations of BCC + FCC, or other TCP phases, for intermediate VEC values. The overall VEC of the prepared alloys and that of the detected phases (all calculated at the corresponding experimental compositions) are reported in Table 10.

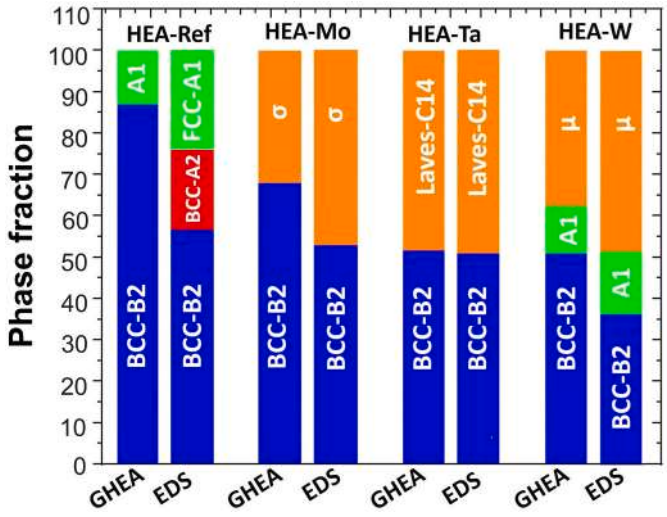

Fig. 10. Comparison between experimental (EDS) and calculated (GHEA) equilibrium phase fraction (EPF) for the four investigated HEAs.

Table 8
Equilibrium phase fraction (EPF, mol%) and compositions of BCC-B2 phase for all the investigated HEAs, evaluated by image analysis and SEM-EDS, respectively.

BCC-B2 phase-mol%							
HEA-X	EPF (mol%)	Al	Co	Cr	Fe	Ni	X
HEA-Ref	57.0	28.6	16.2	7.3	12.7	34.4	–
HEA-Mo	53.0	27.8	18.3	9.0	14.5	27.9	2.5
HEA-Ta	51.2	34.2	15.1	8.8	10.5	28.8	2.6
HEA-W	37.0	28.6	16.2	7.3	12.7	34.4	0.7

Table 9
Equilibrium phase fractions (EPF, mol%) and compositions of the TCP phases for all the investigated HEAs, evaluated by image analysis and SEM-EDS, respectively.

TCP phase-mol%								
HEA-X	TCP phase	EPF (mol %)	Al	Co	Cr	Fe	Ni	X
HEA-Mo	σ	47.0	5.2	17.7	27.4	20.6	7.8	21.2
HEA-Ta	Laves-C14	48.5	3.5	17.7	22.4	21.3	7.2	27.8
HEA-W	μ	46.6	1.7	17.1	18.7	16.0	6.7	39.8

It can be observed that overall VEC values range from 6.93 for HEA-Ta to 7.33 for HEA-W. Additionally, in agreement with Guo et al. [60].

a) none of the samples prepared in this work is monophasic;
b) FCC is present in the samples with the higher VEC (HEA-W and HEA-Ref);
c) the FCC/BCC molar ratio is higher in the sample with higher VEC.

In the samples containing a refractory metal, the formation of an intermetallic (IM) is promoted. In particular, Mo and W additions respectively stabilize σ and μ (typical VEC stabilized phases), which actually show their characteristic VEC values approximately in the 6.5–7.5 range.

As for the Laves-C14 phase, Stein and Leineweber observed that in HEAs it usually coexists with BCC solid solution for VEC < 7 and with FCC solid solution for VEC > 7 [61]. This well applies to the present HEA-Ta sample, with an overall VEC = 6.93, where the BCC + Laves-C14 two-phase field was observed.

4.2. Microhardness measurements

Microhardness measurements were performed on cross-sectioned samples as an additional contribution to the phase characterization (Fig. 11). Additionally, larger indentations at higher loads (0.1 kgf) were performed encompassing all the phases in each sample, to have an estimation of the alloy overall microhardness. The values of 504HV0.1 ± 8, 766HV0.1 ± 20, 921HV0.1 ± 22 and 890HV0.1 ± 13 were obtained for HEA-Ref, HEA-Mo, HEA-Ta, and HEA-W, respectively (Fig. 11a). This indicates a significant overall microhardness increase in the alloys due to the introduction of the refractory element.

Even though care should be taken in comparing microhardness values for HEAs prepared with different procedures and annealed at different temperatures and times, good agreement with literature data on equiatomic AlCoCrFeNi HEAs was obtained for HEA-Ref [62–64]. The presence of the soft FCC phase accounts for its lower microhardness, since FCC phases are generally associated with lower hardness than that of the BCC phases [65]. On the other hand, the addition of a refractory element to HEA-Ref, led to the formation of TCP phases, resulting in significant overall hardening, as also observed in Ref. [66].

For all the samples, the overall microhardness evaluated on large areas (Fig. 11a) reflects the sum of the relative contributions from each phase, as measured on smaller areas and reported in Fig. 11b. As for the microhardness of the single phases, the relatively low scatter of data (Fig. 11b) results from the homogeneity of the microstructures, underlining the effectiveness of the long annealing. Nevertheless, microhardness values for some of the investigated phases could not be isolated from the contributions of their surroundings, because they were too intimately mixed (FCC-A1+BCC-A2 in HEA-Ref) or because of their small crystal dimensions (G' phase in HEA-Ta, Fig. 6a). For the BCC-B2 phase, common to all the alloys, no significant variation in HV was found regardless of the contained refractory element, the composition, and the type of secondary phase. As expected, TCP phases resulted noticeably harder than the main B2-based solid solutions, with HV(μ) > HV(σ) > HV(Laves-C14).

5. Conclusions

Four HEAs, namely AlCoCrFeNi (HEA-Ref), AlCoCrFeNiMo (HEA-Mo), AlCoCrFeNiTa (HEA-Ta) and AlCoCrFeNiW (HEA-W), were synthesized and heat treated according to the predictions of the GHEA thermodynamic database, able to calculate phase equilibria in the senary Al–Co–Cr–Fe–Ni-X (X = Mo, Ta, W) systems. To the best of our knowledge no experimental information about such equimolar alloys was available in literature. Alloy samples were then characterized by

Table 10
Amount and VEC of the HEAs synthesized in this work and of the phases formed in each of them.

Sample	Overall VEC	BCC mol%	BCC VEC	FCC mol%	FCC VEC	FCC/BCC ratio	IM mol%	IM VEC	IM phase
HEA-W	7.33	37	7.25	16	7.76	0.43	47	7.05	μ
HEA-Ref	7.24	77(*)	6.95	23	8.33	0.30	–	–	–
HEA-Mo	7.07	53	7.12	–	–	–	47	7.09	σ
HEA-Ta	6.93	51	6.76	–	–	–	49	6.86	C14

(*) Phase amount refers to the sum of B2+A2 phases.

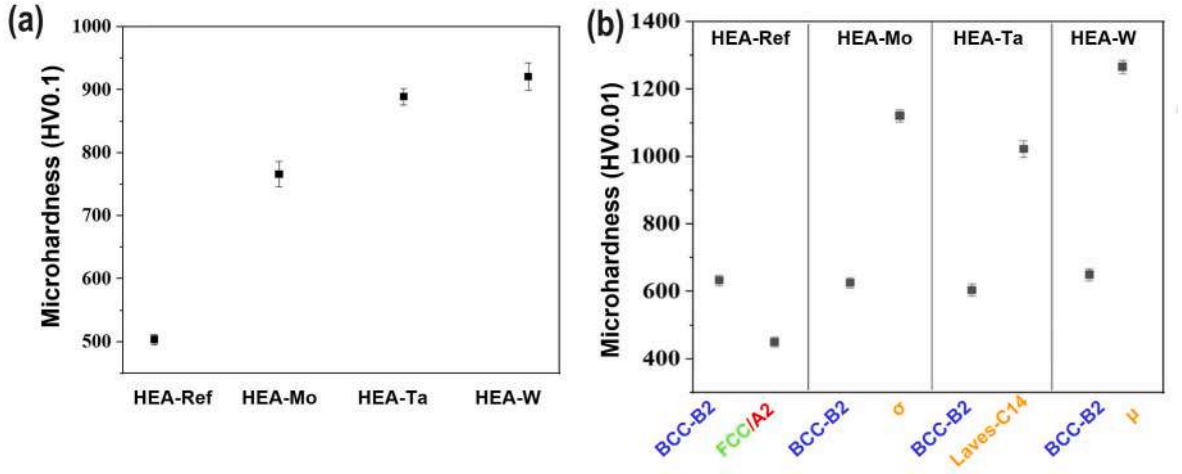

Fig. 11. Overall microhardness measurements performed on cross-sectioned samples with a load of 0.1 kgf (a); HV values for each phase evaluated with a load of 0.01 kgf (b).

SEM-EDS, XRD and micro-hardness measurements to, in turn, contribute validating the GHEA database itself.

The main outcomes of the present work are listed below.

- Despite the difficult preparation, homogeneous microstructures were obtained for all the alloy samples after appropriate synthesis and heat treatment.
- HEA-Ref showed a 3-phase microstructure formed by BCC-A2, BCC-B2 and FCC-A1, with no TCP phases; the addition of Mo, Ta, and W led to the formation of σ, Laves-C14 and μ phases, respectively.
- The agreement between experimental results (phase identification by XRD and analysis by SEM-EDS) and calculations (equilibrium phases and their compositions) is generally satisfactory, and it qualitatively validates the GHEA thermodynamic database. Some discrepancies between experimental and calculated compositions of the TCP phases suggest the need for an improvement of the metastable endmember parameters for such phases. To this end, however, comparison with more experimental data is required.
- VEC-based phase stabilization criteria proposed in the literature are confirmed by the present phase analysis results. Such criteria can be used as a qualitative contribution to the validation of CALPHAD predictions.
- Microhardness measurements, while not directly related to phase equilibria, constitute a useful additional information in view of possible applications of the alloys considered in this work. In particular, they show that the microhardness of BCC-B2, the only phase common to all the prepared HEAs, does not appreciably change with the addition of the refractory element. Such additions cause an increase of the overall alloy micro-hardness by promoting the formation of the harder TCP phases. On the contrary, HEA-Ref, the only sample where FCC is present, shows the lowest microhardness.

Future developments include the improvement of the predictive power of GHEA, especially regarding phase compositions. In this sense, the availability of a higher amount of experimental data on such systems at high refractory concentrations is needed. The present work, together with an upcoming paper of the same authors on Al–Co–Cr–Fe–Ni-X-C (X = Mo, Ta) systems, contributes to the continuous validation of the GHEA thermodynamic database.

CRediT authorship contribution statement

S. Gambaro: Writing – review & editing, Writing – original draft, Methodology, Investigation, Formal analysis, Data curation, Conceptualization. **L. Fenocchio:** Writing – review & editing, Methodology, Investigation, Formal analysis, Data curation, Conceptualization. **F. Valenza:** Writing – review & editing, Supervision, Methodology, Investigation, Funding acquisition, Formal analysis, Data curation, Conceptualization. **P. Riani:** Investigation, Formal analysis. **G. Cacciamani:** Writing – review & editing, Supervision, Methodology, Investigation, Funding acquisition, Formal analysis, Data curation, Conceptualization.

Declaration of competing interest

The authors declare that they have no known competing financial interests or personal relationships that could have appeared to influence the work reported in this paper.

Data availability

Data will be made available on request.

References

[1] S.K. Dewangan, A. Mangish, S. Kumar, A. Sharma, B. Ahn, V. Kumar, A review on High-Temperature Applicability: a milestone for high entropy alloys, Eng. Sci. Technol. Int. J. 35 (Nov. 2022) 101211, https://doi.org/10.1016/j.jestch.2022.101211.

[2] Z. Tang, et al., Tensile ductility of an AlCoCrFeNi multi-phase high-entropy alloy through hot isostatic pressing (HIP) and homogenization, Mater. Sci. Eng., A 647 (Oct. 2015) 229–240, https://doi.org/10.1016/j.msea.2015.08.078.

[3] Y.J. Zhou, Y. Zhang, Y.L. Wang, G.L. Chen, Solid solution alloys of $AlCoCrFeNiTi_x$ with excellent room-temperature mechanical properties, Appl. Phys. Lett. 90 (18) (Apr. 2007) 181904, https://doi.org/10.1063/1.2734517.

[4] C.-Y. Hsu, C.-C. Juan, W.-R. Wang, T.-S. Sheu, J.-W. Yeh, S.-K. Chen, On the superior hot hardness and softening resistance of $AlCoCr_xFeMo_{0.5}Ni$ high-entropy alloys, Mater. Sci. Eng., A 528 (10–11) (Apr. 2011) 3581–3588, https://doi.org/10.1016/j.msea.2011.01.072.

[5] C.M. Liu, H.M. Wang, S.Q. Zhang, H.B. Tang, A.L. Zhang, Microstructure and oxidation behavior of new refractory high entropy alloys, J. Alloys Compd. 583 (Jan. 2014) 162–169, https://doi.org/10.1016/j.jallcom.2013.08.102.

[6] M.-H. Chuang, M.-H. Tsai, W.-R. Wang, S.-J. Lin, J.-W. Yeh, Microstructure and wear behavior of $Al_xCo_{1.5}CrFeNi_{1.5}Ti_y$ high-entropy alloys, Acta Mater. 59 (16) (Sep. 2011) 6308–6317, https://doi.org/10.1016/j.actamat.2011.06.041.

[7] Y. Zhang, et al., Microstructures and properties of high-entropy alloys, Prog. Mater. Sci. 61 (Apr. 2014) 1–93, https://doi.org/10.1016/j.pmatsci.2013.10.001.

[8] O.N. Senkov, G.B. Wilks, J.M. Scott, D.B. Miracle, Mechanical properties of Nb25Mo25Ta25W25 and V20Nb20Mo20Ta20W20 refractory high entropy alloys, Intermetallics 19 (5) (May 2011) 698–706, https://doi.org/10.1016/j.intermet.2011.01.004.

[9] Y.P. Wang, B.S. Li, M.X. Ren, C. Yang, H.Z. Fu, Microstructure and compressive properties of AlCrFeCoNi high entropy alloy, Mater. Sci. Eng., A 491 (1–2) (Sep. 2008) 154–158, https://doi.org/10.1016/j.msea.2008.01.064.

[10] M. Tokarewicz, M. Grądzka-Dahlke, Review of recent research on AlCoCrFeNi high-entropy alloy, Metals 11 (8) (Aug. 2021) 1302, https://doi.org/10.3390/met11081302.

[11] Y.X. Zhuang, X.L. Zhang, X.Y. Gu, Effect of molybdenum on phases, microstructure and mechanical properties of $Al_{0.5}$CoCrFeMo Ni high entropy alloys, J. Alloys Compd. 743 (Apr. 2018) 514–522, https://doi.org/10.1016/j.jallcom.2018.02.003.

[12] H. Jiang, K. Han, D. Qiao, Y. Lu, Z. Cao, T. Li, Effects of Ta addition on the microstructures and mechanical properties of CoCrFeNi high entropy alloy, Mater. Chem. Phys. 210 (May 2018) 43–48, https://doi.org/10.1016/j.matchemphys.2017.05.056.

[13] T.-T. Shun, L.-Y. Chang, M.-H. Shiu, Microstructure and mechanical properties of multiprincipal component CoCrFeNiMo$_x$ alloys, Mater. Char. 70 (Aug. 2012) 63–67, https://doi.org/10.1016/j.matchar.2012.05.005.

[14] C. Ai, et al., Alloy design, micromechanical and macromechanical properties of CoCrFeNiTa$_x$ eutectic high entropy alloys, J. Alloys Compd. 735 (Feb. 2018) 2653–2662, https://doi.org/10.1016/j.jallcom.2017.12.015.

[15] W. Huo, H. Zhou, F. Fang, X. Zhou, Z. Xie, J. Jiang, Microstructure and properties of novel CoCrFeNiTa$_x$ eutectic high-entropy alloys, J. Alloys Compd. 735 (Feb. 2018) 897–904, https://doi.org/10.1016/j.jallcom.2017.11.075.

[16] M.J. Kim, et al., Understanding microstructure and mechanical properties of ($AlTa_{0.76}$) CoCrFeNi$_{2.1}$ eutectic high entropy alloys via thermo-physical parameters, J. Mater. Sci. Technol. 57 (Nov. 2020) 131–137, https://doi.org/10.1016/j.jmst.2020.03.045.

[17] F. Ge, et al., Microstructure, hardness and wear resistance of AlCoCrFeNiTa$_x$ (x = 0, 0.1, 0.3) high-entropy alloys enhanced by laser remelting and Ta addition, J. Alloys Compd. 949 (Jul. 2023) 169741, https://doi.org/10.1016/j.jallcom.2023.169741.

[18] P. Wang, Y. Wang, F. Cui, X. Yang, A. Pan, W. Wu, Microstructural evolution, mechanical properties and corrosion resistance of CoCrFeNiW$_{0.5}$ high entropy alloys with various annealing heat treatment, J. Alloys Compd. 918 (Oct. 2022) 165602, https://doi.org/10.1016/j.jallcom.2022.165602.

[19] Z. Niu, J. Xu, T. Wang, N. Wang, Z. Han, Y. Wang, Microstructure, mechanical properties and corrosion resistance of CoCrFeNiW (x = 0, 0.2, 0.5) high entropy alloys, Intermetallics 112 (Sep. 2019) 106550, https://doi.org/10.1016/j.intermet.2019.106550.

[20] Y. Dong, Y. Lu, Effects of tungsten addition on the microstructure and mechanical properties of near-eutectic AlCoCrFeNi$_2$ high-entropy alloy, J. Mater. Eng. Perform. 27 (1) (Jan. 2018) 109–115, https://doi.org/10.1007/s11665-017-3096-6.

[21] Y. Dong, Y. Lu, Microstructure and mechanical properties of CoCrFeNi$_2$Al$_{1-x}$W$_x$ high entropy alloys, Arabian J. Sci. Eng. 44 (2) (Feb. 2019) 803–808, https://doi.org/10.1007/s13369-018-3297-9.

[22] J.E. Saal, I.S. Berglund, J.T. Sebastian, P.K. Liaw, G.B. Olson, Equilibrium high entropy alloy phase stability from experiments and thermodynamic modeling, Scripta Mater. 146 (Mar. 2018) 5–8, https://doi.org/10.1016/j.scriptamat.2017.10.027.

[23] C. Zhang, F. Zhang, S. Chen, W. Cao, Computational thermodynamics aided high-entropy alloy design, J. Miner. Met. Mater. Soc. 64 (7) (Jul. 2012) 839–845, https://doi.org/10.1007/s11837-012-0365-6.

[24] O.N. Senkov, S. Gorsse, D.B. Miracle, High temperature strength of refractory complex concentrated alloys, Acta Mater. 175 (Aug. 2019) 394–405, https://doi.org/10.1016/j.actamat.2019.06.032.

[25] M. Wu, S. Wang, H. Huang, D. Shu, B. Sun, CALPHAD aided eutectic high-entropy alloy design, Mater. Lett. 262 (Mar. 2020) 127175, https://doi.org/10.1016/j.matlet.2019.127175.

[26] C. Zhang, Y. Yang, The CALPHAD approach for HEAs: challenges and opportunities, MRS Bull. 47 (2) (Feb. 2022) 158–167, https://doi.org/10.1557/s43577-022-00284-8.

[27] Y. Wang, M. Ostrowska, G. Cacciamani, Thermodynamic modeling of selected ternary systems containing Y and CALPHAD simulation of CoNiCrAlY metallic coatings, Calphad 72 (Mar. 2021) 102214, https://doi.org/10.1016/j.calphad.2020.102214.

[28] G. Cacciamani, G. Roncallo, Y. Wang, E. Vacchieri, A. Costa, Thermodynamic modelling of a six component (C-Co-Cr-Ni-Ta-W) system for the simulation of Cobalt based alloys, J. Alloys Compd. 730 (Jan. 2018) 291–310, https://doi.org/10.1016/j.jallcom.2017.09.327.

[29] M. Ostrowska, P. Riani, B. Bocklund, Z.-K. Liu, G. Cacciamani, Thermodynamic modeling of the Al-Co-Cr-Fe-Ni high entropy alloys supported by key experiments, J. Alloys Compd. 897 (Mar. 2022) 162722, https://doi.org/10.1016/j.jallcom.2021.162722.

[30] L. Fenocchio, G. Cacciamani, Validation and application of the Genova high-entropy alloys (GHEA) thermodynamic database for selected multi-component systems, in: Oral Communication, CALPHAD L Conference on Computer Coupling of Phase Diagrams and Thermochemistry, MIT Cambridge, Boston (USA), 2023.

[31] M. Ostrowska, PhD. Thesis, Thermodynamic modelling and experimental validation of High Entropy Alloys containing Al, Co, Ce, Fe, Mo, Ni, Ta and W for high-temperature applications, Università degli Studi di Genova (2021).

[32] D.M. Cupid, O. Fabrichnaya, F. Ebrahimi, H.J. Seifert, Thermodynamic assessment of the Al–Mo system and of the Ti–Al–Mo System from 0 to 20at.% Ti, Intermetallics 18 (6) (Jun. 2010) 1185–1196, https://doi.org/10.1016/j.intermet.2010.03.010.

[33] J. Peng, P. Franke, D. Manara, T. Watkins, R.J.M. Konings, H.J. Seifert, Experimental investigation and thermodynamic re-assessment of the Al–Mo–Ni system, J. Alloys Compd. 674 (Jul. 2016) 305–314, https://doi.org/10.1016/j.jallcom.2016.03.044.

[34] V.T. Witusiewicz, et al., Experimental study and thermodynamic re-assessment of the binary Al–Ta system, Intermetallics 18 (1) (Jan. 2010) 92–106, https://doi.org/10.1016/j.intermet.2009.06.015.

[35] P. Wang, et al., Thermodynamic re-assessment of the Al-Co-W system, Calphad 59 (Dec. 2017) 112–130, https://doi.org/10.1016/j.calphad.2017.09.007.

[36] A. Davydov, U.R. Kattner, Thermodynamic assessment of the Co-Mo system, J. Phase Equil. 20 (1) (Jan. 1999) 5–16, https://doi.org/10.1361/105497199770335893.

[37] Z. Du, C. Guo, C. Li, W. Zhang, Thermodynamic description of the Al-Mo and Al-Fe-Mo systems, J. Phase Equilibria Diffus. 30 (5) (Oct. 2009) 487–501, https://doi.org/10.1007/s11669-009-9564-4.

[38] C. Zhou, C. Guo, C. Li, Z. Du, Thermodynamic description of the Co–Ni–Ta system, Calphad 66 (Sep. 2019) 101649, https://doi.org/10.1016/j.calphad.2019.101649.

[39] V.T. Witusiewicz, et al., Experimental study and thermodynamic modelling of the ternary Al–Fe–Ta system, J. Mater. Sci. 48 (1) (Jan. 2013) 377–412, https://doi.org/10.1007/s10853-012-6755-x.

[40] K. Frisk, A thermodynamic evaluation of the Cr-N, Fe-N, Mo-N and Cr-Mo-N systems, Calphad 15 (1) (Jan. 1991) 79–106, https://doi.org/10.1016/0364-5916(91)90028-I.

[41] J. Zhu, M.S. Titus, T.M. Pollock, Experimental investigation and thermodynamic modeling of the Co-rich region in the Co-Al-Ni-W quaternary system, J. Phase Equilibria Diffus. 35 (5) (Oct. 2014) 595–611, https://doi.org/10.1007/s11669-014-0327-5.

[42] N. Dupin, I. Ansara, Thermodynamic assessment of the Cr-Ta system, J. Phase Equil. 14 (4) (Aug. 1993) 451–456, https://doi.org/10.1007/BF02671963.

[43] J. Pavlů, J. Vřešťál, M. Šob, Re-modeling of Laves phases in the Cr–Nb and Cr–Ta systems using first-principles results, Calphad 33 (1) (Mar. 2009) 179–186, https://doi.org/10.1016/j.calphad.2008.04.006.

[44] W. Wang, F. Yin, M. Zhang, M. Zhao, Z. Li, Experimental investigation and thermodynamic calculation of the Co-Cr-Mo system, J. Phase Equilibria Diffus. 35 (5) (Oct. 2014) 544–554, https://doi.org/10.1007/s11669-014-0317-7.

[45] P. Gustafson, An experimental study and a thermodynamic evaluation of the Cr-Fe-W system, Metall. Trans. A 19 (10) (Oct. 1988) 2531–2546, https://doi.org/10.1007/BF02645481.

[46] V.B. Rajkumar, K.C. Hari Kumar, Thermodynamic modeling of the Fe–Mo system coupled with experiments and ab initio calculations, J. Alloys Compd. 611 (Oct. 2014) 303–312, https://doi.org/10.1016/j.jallcom.2014.05.030.

[47] V.T. Witusiewicz, A.A. Bondar, U. Hecht, T.Y. Velikanova, Phase equilibria in binary and ternary systems with chemical and magnetic ordering, J. Phase Equilibria Diffus. 32 (4) (Aug. 2011) 329–349, https://doi.org/10.1007/s11669-011-9910-1.

[48] E. Povoden-Karadeniz, E. Eidenberger, P. Lang, G. Stechauner, H. Leitner, E. Kozeschnik, Simulation of precipitate evolution in Fe–25 Co– 15 Mo with Si addition based on computational thermodynamics, J. Alloys Compd. 587 (Feb. 2014) 158–170, https://doi.org/10.1016/j.jallcom.2013.10.166.

[49] A. Jacob, C. Schmetterer, L. Singheiser, A. Gray-Weale, B. Hallstedt, A. Watson, Modeling of Fe–W phase diagram using first principles and phonons calculations, Calphad 50 (Sep. 2015) 92–104, https://doi.org/10.1016/j.calphad.2015.04.010.

[50] A.F. Guillermet, The Co-Fe-Ni-W-C Phase Diagram: A Thermodynamic Description and Calculated Sections for (Co-Fe-Ni) Bonded Cemented WC Tools/Das Co-Fe-Ni-W-C Zustandsdiagramm: Eine thermodynamische Beschreibung und berechnete Schnitte für Co-Fe-Ni-gebundene Hartmetall-WC-Werkzeuge, Int. J. Mater. Res. 80 (2) (Feb. 1989) 83–94, https://doi.org/10.1515/ijmr-1989-800204.

[51] S.H. Zhou, Y. Wang, C. Jiang, J.Z. Zhu, L.-Q. Chen, Z.-K. Liu, First-principles calculations and thermodynamic modeling of the Ni–Mo system, Mater. Sci. Eng., A 397 (1–2) (Apr. 2005) 288–296, https://doi.org/10.1016/j.msea.2005.02.037.

[52] C. Zhang, Y. Liu, Y. Du, Y. Peng, J. Wang, Thermodynamic assessment of the Co–Mo–Ni and Mo–Ni–W ternary systems, Calphad 55 (Dec. 2016) 243–251, https://doi.org/10.1016/j.calphad.2016.10.001.

[53] S.H. Zhou, Y. Wang, L.-Q. Chen, Z.-K. Liu, R.E. Napolitano, Solution-based thermodynamic modeling of the Ni–Ta and Ni–Mo–Ta systems using first-principle calculations, Calphad 33 (4) (Dec. 2009) 631–641, https://doi.org/10.1016/j.calphad.2009.06.006.

[54] A.F. Guillermet, L. Östlund, Experimental and theoretical study of the phase equilibria in the fe-ni-w system, Metall. Trans. A 17 (10) (Oct. 1986) 1809–1823, https://doi.org/10.1007/BF02817278.

[55] P. Gustafson, A thermodynamic evaluation of the Cr-Ni-W system, Calphad 12 (3) (1988) 277–292.

[56] S. Gambaro, et al., High-temperature-reactivity of Al–Ti alloys in contact with SiC, J. Alloys Compd. 817 (Mar. 2020) 152715, https://doi.org/10.1016/j.jallcom.2019.152715.

[57] S. Gambaro, F. Valenza, M.L. Muolo, A. Passerone, G. Cacciamani, Wettability of SiC and graphite by Co–Ta alloys: evaluation of the reactivity supported by thermodynamic calculations, J. Mater. Sci. 52 (23) (Dec. 2017) 13414–13426, https://doi.org/10.1007/s10853-017-1448-0.

[58] F. Valenza, S. Gambaro, M.L. Muolo, M. Salvo, V. Casalegno, Wetting of SiC by Al-Ti alloys and joining by in-situ formation of interfacial Ti3Si(Al)C2, J. Eur. Ceram. Soc. 38 (11) (Sep. 2018) 3727–3734, https://doi.org/10.1016/j.jeurceramsoc.2018.04.025.

[59] S. Gambaro, F. Valenza, M.L. Muolo, A. Passerone, P. Riani, G. Cacciamani, Zirconia-high entropy alloys joints for biomedical applications: the role of Ag-based fillers on interfacial reactivity, J. Alloys Compd. 909 (Jul. 2022) 164764, https://doi.org/10.1016/j.jallcom.2022.164764.

[60] S. Guo, C. Ng, J. Lu, C.T. Liu, Effect of valence electron concentration on stability of fcc or bcc phase in high entropy alloys, J. Appl. Phys. 109 (10) (May 2011), https://doi.org/10.1063/1.3587228.

[61] F. Stein, A. Leineweber, Laves phases: a review of their functional and structural applications and an improved fundamental understanding of stability and properties, J. Mater. Sci. 56 (9) (Mar. 2021) 5321–5427, https://doi.org/10.1007/s10853-020-05509-2.

[62] A. Munitz, S. Salhov, S. Hayun, N. Frage, Heat treatment impacts the microstructure and mechanical properties of AlCoCrFeNi high entropy alloy, J. Alloys Compd. 683 (Oct. 2016) 221–230, https://doi.org/10.1016/j.jallcom.2016.05.034.

[63] W. Ji, et al., Mechanical alloying synthesis and spark plasma sintering consolidation of CoCrFeNiAl high-entropy alloy, J. Alloys Compd. 589 (Mar. 2014) 61–66, https://doi.org/10.1016/j.jallcom.2013.11.146.

[64] M. López Ríos, et al., Effects of nickel content on the microstructure, microhardness and corrosion behavior of high-entropy AlCoCrFeNix alloys, Sci. Rep. 10 (1) (Dec. 2020) 21119, https://doi.org/10.1038/s41598-020-78108-5.

[65] D. Beniwal, P. Singh, S. Gupta, M.J. Kramer, D.D. Johnson, P.K. Ray, Distilling physical origins of hardness in multi-principal element alloys directly from ensemble neural network models, npj Comput. Mater. 8 (1) (Jul. 2022) 153, https://doi.org/10.1038/s41524-022-00842-3.

[66] M.-H. Tsai, et al., Significant hardening due to the formation of a sigma phase matrix in a high entropy alloy, Intermetallics 33 (Feb. 2013) 81–86, https://doi.org/10.1016/j.intermet.2012.09.022.